Available online at www.sciencedirect.com
ScienceDirect
Journal of Computational Physics 227 (2008) 3405–3427
JOURNAL OF COMPUTATIONAL PHYSICS
www.elsevier.com/locate/jcp

Increasing the accuracy in locally divergence-preserving finite volume schemes for MHD

Robert Artebrant *, Manuel Torrilhon

Seminar for Applied Mathematics, ETH Zentrum, Rämistrasse 101, 8092 Zurich, Switzerland

Received 30 April 2007; received in revised form 5 December 2007; accepted 6 December 2007
Available online 23 December 2007

Abstract

It is of utmost interest to control the divergence of the magnetic flux in simulations of the ideal magnetohydrodynamic equations since, in general, divergence errors tend to accumulate and render the schemes unstable. This paper presents a higher-order extension of the locally divergence-preserving procedure developed in Torrilhon [M. Torrilhon, Locally divergence-preserving upwind finite volume schemes for magnetohydrodynamic equations, SIAM J. Sci. Comput. 26 (2005) 1166–1191]; a fourth-order accurate local redistribution of the numerical magnetic field fluxes of a finite volume base scheme is introduced. The redistribution ensures that a fourth-order accurate discrete divergence operator is preserved to round off errors when applied to the cell averages of the magnetic flux density. The developed procedure is applicable to generic semi-discrete finite volume schemes and its purpose is to stabilize the schemes using a local procedure that respects the accuracy of the base scheme to a greater extent than the previous second-order achievements. Numerical experiments that demonstrate the properties of the new procedure are also presented.

AMS: 35L65; 35L45; 65M06; 76N15

Keywords: Magnetohydrodynamics; Divergence constraint; Finite volume method; High-order reconstruction

1. Introduction

Violation of the divergence constraint on the magnetic flux density in magnetohydrodynamical (MHD) simulations leads to stability problems and it is therefore of great importance to numerically respect this intrinsic constraint. Approaches suggested in the literature to satisfy the divergence constraint include: divergence cleaning by solving an elliptic problem [5], advecting the divergence errors out of the domain by writing the MHD-system with an additional source term [14] (see also [7]), and special discretizations of the equations for the magnetic field [8,20,4]. Also filtering methods like in [13] can be applied.

* Corresponding author.
E-mail addresses: robert.artebrant@sam.math.ethz.ch (R. Artebrant), manuel.torrilhon@sam.math.ethz.ch (M. Torrilhon).

0021-9991/$ - see front matter © 2007 Elsevier Inc. All rights reserved.
doi:10.1016/j.jcp.2007.12.003

Since the divergence preservation is a local phenomenon inherent in the MHD-system it is appealing to mimic this property numerically by a locally divergence-preserving scheme. Moreover, a conservative scheme is preferred for the approximation of discontinuous solutions. A very interesting approach of this type was advocated in [18,19]. These papers present a framework for the construction of a local procedure to *redistribute* the numerical fluxes in a finite volume (FV) scheme, so that a discrete divergence operator vanishes. The procedure stabilizes the base scheme and respects the accuracy to the second-order level. With the current availability of higher-order FV-schemes, however, one would like to increase the accuracy of the divergence-preserving procedure.

In the present paper a development of the procedure in [18] is carried out leading to a procedure that still complies with the finite volume framework, but now preserves a fourth-order discrete divergence operator locally and, furthermore, retains the accuracy of a generic semi-discrete finite volume scheme up to fourth order. The redistribution of the numerical magnetic field fluxes can still be formulated in a standard conservative setting which makes implementation of the divergence-preserving modification in an existing FV-scheme convenient.

The paper is organized as follows. In the next section the finite volume base schemes used in this paper for approximation of the ideal MHD-system are described. Section 3 presents the derivation of the divergence-preserving procedure. This is followed by a section containing numerical experiments. Finally, a summary concludes the paper.

2. Base schemes

The 2-D ideal magnetohydrodynamic equations constitute a system of conservation laws

$$u(x,y,t)_t + F(u(x,y,t))_x + G(u(x,y,t))_y = 0, \tag{1}$$

where, see e.g. [12]

$$u = (\rho, \rho v_x, \rho v_y, \rho v_z, B_x, B_y, B_z, \epsilon)^{\mathrm{T}}, \tag{2}$$

$$\begin{aligned} F = (&\rho v_x, \rho v_x^2 + p^* - B_x^2, \rho v_x v_y - B_x B_y, \rho v_x v_z - B_x B_z, 0, v_x B_y - v_y B_x, \\ &v_x B_z - v_z B_x, v_x(\epsilon + p^*) - B_x(v_x B_x + v_y B_y + v_z B_z))^{\mathrm{T}}, \end{aligned} \tag{3}$$

and

$$\begin{aligned} G = (&\rho v_y, \rho v_y v_x - B_y B_x, \rho v_y^2 + p^* - B_y^2, \rho v_y v_z - B_y B_z, v_y B_x - v_x B_y, \\ &0, v_y B_z - v_z B_y, v_y(\epsilon + p^*) - B_y(v_x B_x + v_y B_y + v_z B_z))^{\mathrm{T}}. \end{aligned} \tag{4}$$

In these expressions $p^* = p + B^2/2, \epsilon = \rho v^2/2 + B^2/2 + p/(\gamma - 1)$ and in this paper the adiabatic constant is $\gamma = 5/3$.

2.1. Finite volume discretization

A semi-discrete finite volume (FV) scheme is obtained by integrating and averaging (1) over computational cells $[x_i - \frac{\Delta x}{2}, x_i + \frac{\Delta x}{2}] \times [y_j - \frac{\Delta y}{2}, y_j + \frac{\Delta y}{2}]$,

$$\begin{aligned} \frac{\mathrm{d}}{\mathrm{d}t}\bar{u}_{ij}(t) = -\frac{1}{\Delta x \Delta y}\Bigg(&\int_{y_{j-1/2}}^{y_{j+1/2}} F(u(x_{i+1/2},y,t))\,\mathrm{d}y - \int_{y_{j-1/2}}^{y_{j+1/2}} F(u(x_{i-1/2},y,t))\,\mathrm{d}y + \int_{x_{i-1/2}}^{x_{i+1/2}} G(u(x,y_{j+1/2},t))\,\mathrm{d}x \\ &- \int_{x_{i-1/2}}^{x_{i+1/2}} G(u(x,y_{j-1/2},t))\,\mathrm{d}x\Bigg), \end{aligned} \tag{5}$$

where

$$\bar{u}_{ij}(t) = \frac{1}{\Delta x \Delta y}\int_{y_{j-1/2}}^{y_{j+1/2}}\int_{x_{i-1/2}}^{x_{i+1/2}} u(x,y,t)\,\mathrm{d}x\,\mathrm{d}y,$$

is the cell average. The FV-discretization approximates (5) by

$$\frac{\mathrm{d}}{\mathrm{d}t}\bar{u}_{ij}(t) = -\frac{1}{\Delta x}\left(\widehat{F}_{i+1/2,j} - \widehat{F}_{i-1/2,j}\right) - \frac{1}{\Delta y}(\widehat{G}_{i,j+1/2} - \widehat{G}_{i,j-1/2}). \tag{6}$$

Here the quantities $\widehat{F}$ and $\widehat{G}$ approximate the line integrals of the fluxes in (5). For example

$$\widehat{F}_{i+1/2,j} = \sum_k w_k \hat{f}(u^-_{i+1/2,y_j+p_k\Delta y}, u^+_{i+1/2,y_j+p_k\Delta y}) \approx \frac{1}{\Delta y}\int_{y_{j-1/2}}^{y_{j+1/2}} F(u(x_{i+1/2}, y, t))\,\mathrm{d}y,$$

where $\hat{f}$ is a one dimensional numerical flux, $u^\pm$ are right/left limits at the cell boundary of *reconstructed* point values of the conserved variable u, and w_k and p_k are weights and nodes of a suitable (Gaussian) quadrature rule.

Reconstructed point values at Gaussian nodes are supplied to the numerical flux by a reconstruction procedure constructed to raise the formal spatial order of the scheme and suppressing oscillations if discontinuities are present.

The divergence-preserving procedure developed in this paper, as well as its second-order version in [18], is not tied to any particular reconstruction or FV-scheme. In this paper we have applied the new procedure in connection with the local double logarithmic reconstruction (LDLR) on rectangles [1]. See Appendix A for a complete description of this reconstruction technique. For the magnetohydrodynamical simulations in this paper the reconstruction is applied component-wise. The semi-discrete FV-scheme (6) with LDLR spatial discretization is integrated in time by the strong stability-preserving Runge–Kutta method SSPRK3 [10] to form a formally third-order accurate scheme.

2.2. Fourth-order scheme for smooth solutions

The divergence-preserving procedure developed in the next section increases the accuracy of the numerical fluxes from the second-order level in [18] to fourth order, given that the fluxes of the base scheme is of that order or higher. A numerical demonstration of the increased accuracy requires therefore a scheme of at least fourth order.

To achieve the fourth-order requirement, a FV-scheme suitable for the approximation of smooth solutions is constructed in the following way. Point values of the conserved variables are obtained by a two dimensional tensor product polynomial of degree four. By requiring that the cell averages of the polynomial is identical to the corresponding cell averages of the conserved variable in a 5×5-neighborhood, we get a fifth-order accurate interpolation in the mid cell [16]. In particular we obtain sufficiently accurate point values for the fourth-order two-point Gaussian rule for integration of the numerical fluxes. Finally, the resulting semi-discrete system (6) is integrated in time by the fourth-order SSPRK(5,4) [17] so that the overall accuracy requirement is reached.

3. Divergence-preserving procedure

We want to find a discrete divergence operator C on a $(2k+1)^2$-stencil that is preserved for a certain distribution of numerical fluxes. The operator C acts on grid functions $u = (u^1, u^2)^{\mathrm{T}}$ and approximates the divergence of u at (x_i, y_j) by

$$C_{ij}u = A_{ij}u^1 + B_{ij}u^2. \tag{7}$$

Here A approximates the x-derivative

$$A_{ij}u^1 = \sum_{m=-k}^{k}\sum_{n=-k}^{k} a_{mn}u^1_{i+m,j+n} = u^1_x(x_i, y_j) + \mathcal{O}(\Delta^p), \tag{8}$$

to some accuracy $\Delta^p = \Delta x^\alpha \Delta y^\beta$, $\alpha + \beta = p$, and B approximates the y-derivative of the other component u^2 similarly.

An important step in the flux distribution schemes in [19,18] is the introduction of a grid shape function Φ having a $(2k+1)^2$-stencil support

$$\Phi(m,n) = \begin{cases} (\phi^1_{mn}, \phi^2_{mn}), & m,n \in \{-k, -k+1, \ldots, k\}, \\ 0, & m,n \notin \{-k, -k+1, \ldots, k\}. \end{cases} \tag{9}$$

This shape function will later be used to redistribute the numerical fluxes and hence we want it to vanish when our divergence operator C acts on it. Due to the finite support of Φ it suffices to solve

$$C_{ij}\Phi = 0, \quad \text{for } i,j = -2k, -2k+1, \ldots, 2k, \tag{10}$$

which is a $(4k+1)^2 \times 2 \cdot (2k+1)^2$ linear system for the $2 \cdot (2k+1)^2$ entries of Φ. The rank of the system (10) will for a fixed k depend on the particular operator (7). A lower rank is preferred since a greater number of non-trivial solutions gives more freedom in constructing a divergence-preserving scheme. If s elements $\Phi^{(i)}$ of the null space of (10) are available, linearity implies that also the linear combination $\sum_{i=1}^{s} c_i \Phi^{(i)}$ satisfies (10) for any scalar c_i. In particular c_i could be fractions of the numerical fluxes at cell boundaries. This fact was exploited in [18] and the linear combination of shape functions with flux coefficients was named a flux distribution.

3.1. The divergence operator

So far the discrete divergence operator has been left unspecified. Our goal in the following is to find an operator that gives rise to a sufficiently large null space of (10), so that there are enough degrees of freedom available to allow for fourth-order accurate numerical fluxes.

In [19] attention was focused on second-order accurate discrete divergence operators, specifically the three-parameter family of symmetric operators on a 3×3-stencil. By varying these parameters and checking their influence on the rank of the system (10) an operator yielding a four-dimensional null space was discovered. This freedom was indeed enough to construct second-order accurate locally divergence-preserving finite volume schemes. No operator generating a larger kernel was found and, unfortunately, imposing higher-order conditions shows that the shape functions in [18] do not provide enough freedom to increase the accuracy beyond the second-order level, see Section 3.6. Consequently, we will in this paper investigate discrete divergence operators on a larger stencil and search for an operator generating a larger null space of (10). Due to symmetry the next step is operators on a 5×5-stencil, which will be the subject of attention in this paper.

Increasing the size of the stencil naturally implies increased complexity of the systems involved. A 3×3-stencil corresponds to $k = 1$ in (8)–(10) and the size of the system (10) is then 25×18. Stepping up to a 5×5-stencil means $k = 2$ and (10) is now a 81×50-system. On a 5×5-stencil it should be feasible to find an adequate fourth-order accurate divergence operator. Now, the increased complexity manifests itself in the larger set of admissible discrete divergence operators. Before proceeding we make the following remark.

Remark 3.1 (*Point values/cell averages*). Finite volume schemes work with cell averages of the conserved variables. For schemes of order three or higher we must distinguish between cell mid point values and cell averages since they only agree to second order. However, if a discrete divergence operator of order p constructed for point values is applied to a grid of cell averages, linearity implies that the cell average of the divergence will be approximated to the same order p.

Thus, in compliance with the finite volume idea, we will construct a discrete divergence operator for point values that will preserve the cell average of the divergence to fourth order, when applied to cell averages.

To build the discretization of the divergence we consider the first derivative in x-direction. On a rectangular, symmetric 5×5 stencil the first derivative in cell (i,j) is calculated from the grid function values by means of (8) with $k = 2$. The classical fourth-order finite difference formula for the first derivative written in stencil notation is

$$A^{\mathrm{cl}} = \frac{1}{12\Delta x}\begin{array}{|c|c|c|c|c|}\hline 0 & 0 & 0 & 0 & 0\\ \hline 0 & 0 & 0 & 0 & 0\\ \hline 1 & -8 & 0 & 8 & -1\\ \hline 0 & 0 & 0 & 0 & 0\\ \hline 0 & 0 & 0 & 0 & 0\\ \hline\end{array}, \tag{11}$$

and satisfies (8) with the order $p = 4$. This, however, is not the only fourth-order accurate first derivative on a two-dimensional 5×5 stencil. Indeed, we can add the weights of discretizations of higher-order derivatives if they produce a value $\mathcal{O}(\Delta^4)$ when divided by Δx. We adopt the notation $\left[\frac{\partial^{p+q}}{\partial x^p \partial y^q}\right]$ for a discretized mixed derivative. Consider, for example the discretization of the mixed fifth derivative

$$\left[\frac{\partial^5}{\partial x \partial y^4}\right] = \frac{1}{12\Delta x\,\Delta y^4}\begin{array}{|c|c|c|c|c|}\hline 1 & -8 & 0 & 8 & -1\\ \hline -4 & 32 & 0 & -32 & 4\\ \hline 6 & -48 & 0 & 48 & -6\\ \hline -4 & 32 & 0 & -32 & 4\\ \hline 1 & -8 & 0 & 8 & -1\\ \hline\end{array}, \tag{12}$$

which gives second-order accuracy in the stencil center. Applying only its weights to a grid function – without the factor involving the grid sizes – we obtain a value proportional to $\Delta x \Delta y^4 \partial_{xyyyy}\psi + \mathcal{O}(\Delta^7)$. Hence, an arbitrary multiple of the weights in the table of (12) can be added to the table in (11) without changing the fourth-order accuracy. The highest one-dimensional derivative that can be represented on a 5×5 stencil has degree four, this limits the possible weights that can be added. Following this argument, the general fourth-order first derivative with a 5×5 stencil acting on u^1 has the form

$$A_{ij}^{\mathrm{gen}} u^1 = \left(A_{ij}^{\mathrm{cl}} + \sum_{p=1}^{4}\sum_{q=p}^{4} \alpha_{pq} \Delta x^{q-1} \Delta y^{4+p-q} \left[\frac{\partial^{4+p}}{\partial x^q \partial y^{4+p-q}}\right]_{ij}\right) u^1 = u_x^1(x_i, y_j) + O(\Delta^4), \tag{13}$$

where $[\cdot]_{ij}$ denotes the unique discretization of the respective derivative obtained from tensorial products. The ten parameters $\alpha_{pq} \in \mathbb{R}$ $(1 \leqslant p \leqslant 4, p \leqslant q \leqslant 4)$ may be chosen arbitrarily without changing the accuracy. The y-derivative is constructed analogously and the combination gives rise to a divergence operator (7). For symmetry we will consider only operators where the weights of the y-derivative follow from the x-derivative by rotation of the grid.

We are looking for a divergence operator which is fourth order and allows a high dimensional null space in the grid. So far, no satisfying theory exists to do this search on the general operator using (13). In principle, we could search for a large null space numerically by scanning through the parameter space given by the α_{pq}. But this parameter space is too large. However, for the case of second-order accuracy it was feasible. There, a similar formula to (13) was constructed with three parameters. The parameter choice that produced a large null space in the second-order case suggests to consider only those mixed derivatives in (13) which are of first degree in x. This reduces the additional weights to a multiple of (12).

With this restriction, the first-order derivative has the form

$$A(\alpha) = \frac{1}{12\Delta x}\begin{array}{|c|c|c|c|c|}\hline 0 & 0 & 0 & 0 & 0\\ \hline 0 & 0 & 0 & 0 & 0\\ \hline 1 & -8 & 0 & 8 & -1\\ \hline 0 & 0 & 0 & 0 & 0\\ \hline 0 & 0 & 0 & 0 & 0\\ \hline\end{array} + \frac{\alpha}{12\Delta x}\begin{array}{|c|c|c|c|c|}\hline 1 & -8 & 0 & 8 & -1\\ \hline -4 & 32 & 0 & -32 & 4\\ \hline 6 & -48 & 0 & 48 & -6\\ \hline -4 & 32 & 0 & -32 & 4\\ \hline 1 & -8 & 0 & 8 & -1\\ \hline\end{array}, \tag{14}$$

where $\alpha \in \mathbb{R}$. From (14) the approximation of the y-derivative is obtained by negating and transposing the stencil. The induced divergence operator can be analyzed through algebra software and we find a nine-dimensional null space of (10) for $\alpha = -\frac{1}{36}$. All other values seem to give only a one-dimensional or (for $\alpha = -\frac{1}{16}$) a four-dimensional null space. The final weights read

$$A\left(-\frac{1}{36}\right) = \frac{1}{432\Delta x}\begin{array}{|c|c|c|c|c|}\hline -1 & 8 & 0 & -8 & 1 \\ \hline 4 & -32 & 0 & 32 & -4 \\ \hline 30 & -240 & 0 & 240 & -30 \\ \hline 4 & -32 & 0 & 32 & -4 \\ \hline -1 & 8 & 0 & -8 & 1 \\ \hline \end{array}, \tag{15}$$

from which the preserved operator is found,

$$C\begin{pmatrix} u^1 \\ u^2 \end{pmatrix} = \frac{1}{432\Delta x}\begin{array}{|c|c|c|c|c|}\hline -1 & 8 & 0 & -8 & 1 \\ \hline 4 & -32 & 0 & 32 & -4 \\ \hline 30 & -240 & 0 & 240 & -30 \\ \hline 4 & -32 & 0 & 32 & -4 \\ \hline -1 & 8 & 0 & -8 & 1 \\ \hline \end{array} u^1 + \frac{1}{432\Delta y}\begin{array}{|c|c|c|c|c|}\hline 1 & -4 & -30 & -4 & 1 \\ \hline -8 & 32 & 240 & 32 & -8 \\ \hline 0 & 0 & 0 & 0 & 0 \\ \hline 8 & -32 & -240 & -32 & 8 \\ \hline -1 & 4 & 30 & 4 & -1 \\ \hline \end{array} u^2. \tag{16}$$

As a comparison we recall the preserved second-order operator from [19,18]

$$C^{2^{\text{nd}}}\begin{pmatrix} u^1 \\ u^2 \end{pmatrix} = \frac{1}{8\Delta x}\begin{array}{|c|c|c|}\hline -1 & 0 & 1 \\ \hline -2 & 0 & 2 \\ \hline -1 & 0 & 1 \\ \hline \end{array} u^1 + \frac{1}{8\Delta y}\begin{array}{|c|c|c|}\hline 1 & 2 & 1 \\ \hline 0 & 0 & 0 \\ \hline -1 & -2 & -1 \\ \hline \end{array} u^2. \tag{17}$$

Now, we turn to the solutions of (10) for the preserved fourth-order operator (16).

3.2. The shape functions

We are interested in shape functions (9) that are the solutions of (10) for the operator (16) found in the previous section. Since this operator gives rise to a nine-dimensional null space we are looking for nine appropriate basis shape functions that will form the building block for the divergence-preserving schemes. Solving the system with Maple it turns out that there exist nine shape functions that all are obtained by mutual translations. The non-vanishing entries of the solutions are

$$\Phi_{mn}(k,l) = \begin{cases} (-\Delta x, -\Delta y), & k = m-1, \;\; l = n+1, \\ (0, -4\Delta y), & k = m-1, \;\; l = n, \\ (\Delta x, -\Delta y), & k = m-1, \;\; l = n-1 \\ (4\Delta x, 0), & k = m, \;\; l = n-1, \\ (\Delta x, \Delta y), & k = m+1, \;\; l = n-1 \\ (0, 4\Delta y), & k = m+1, \;\; l = n, \\ (-\Delta x, \Delta y), & k = m+1, \;\; l = n+1, \\ (-4\Delta x, 0), & k = m, \;\; l = n+1, \end{cases} \tag{18}$$

in their reference 5×5-stencil with cell indices $k, l \in \{-2, \ldots, 2\}$ and for $m, n \in \{-1, 0, 1\}$. The basis shape functions Φ_{mn} describe simple closed loops, with centers at cell indices (m, n), on the nine 3×3-stencils

contained in the 5×5-stencil. Any divergence-preserving solution for (16) can be written as a linear combination of these solutions. Translated shape functions can be defined and evaluated by coming back to the local reference stencil, since the property

$$\Phi_{mn}(k,l) = \Phi_{00}(k-m, l-n), \tag{19}$$

holds for arbitrary indices under the definition

$$\Phi_{00}(k,l) = (0,0)^{\mathrm{T}}, \quad \text{if } k \notin \{-2,\dots,2\} \text{ and/or } l \notin \{-2,\dots,2\}.$$

Property (19) will later be used to construct the divergence preserving procedure.

The structure of the solutions is analogous to the structure of the ones in [19], where the four shape functions describe closed loops on the four interior 2×2-stencils contained in the 3×3-stencil. We notice, however, that (18) cannot be obtained by any linear combination of the shape functions in [19], where we have e.g. the shape function

$$\Phi^{2\text{nd}}_{1/2,1/2}(k,l) = \begin{cases} (-\Delta x, -\Delta y), & k=0, \ l=1, \\ (\Delta x, -\Delta y), & k=0, \ l=0, \\ (\Delta x, \Delta y), & k=1, \ l=0, \\ (-\Delta x, \Delta y), & k=1, \ l=1. \end{cases} \tag{20}$$

Hence, (18) will not preserve the second-order operator (17). A representative of the null space is shown on the left hand side of Fig. 1 in comparison to that of the second-order case.

3.3. The flux distributions

We begin this section by considering the part of a first-order FV-scheme that updates the magnetic flux density. In two dimensions the relevant components for the divergence are $B = (B_x, B_y)^{\mathrm{T}}$ and the scheme reads

$$B^{n+1}_{ij} = B^n_{ij} - \frac{\Delta t}{\Delta x}(F_{i+1/2,j} - F_{i-1/2,j}) - \frac{\Delta t}{\Delta y}(G_{i,j+1/2} - G_{i,j-1/2}). \tag{21}$$

As is evident from the MHD-system (1), the numerical fluxes will differ only in sign and in which component they affect,

$$\begin{aligned} F_{i+1/2,j} &= (0, f_{i+1/2,j})^{\mathrm{T}}, \\ G_{i,j+1/2} &= (g_{i,j+1/2}, 0)^{\mathrm{T}}, \end{aligned} \tag{22}$$

with underlying scalar functions $f = -g$.

The flux distribution schemes introduced in [18] come naturally in the form

$$B^{n+1}_{ij} = B^n_{ij} - \frac{\Delta t}{\Delta x \Delta y} R_{ij}, \tag{23}$$

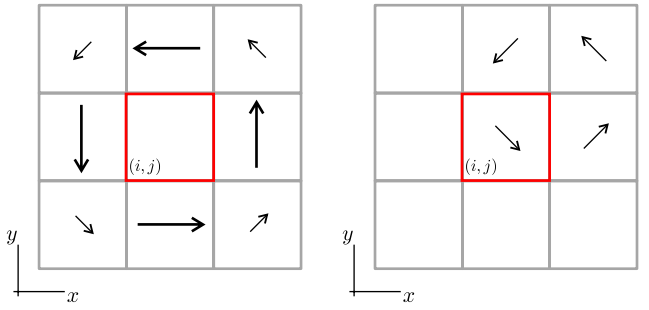

Fig. 1. Null spaces of the fourth-order divergence operator (left) in comparison to the second-order case (right).

for the update of the magnetic flux density B_{ij}. The residual $R = (R^1, R^2)^{\mathrm{T}}$ is formulated in terms of flux distributions and these will be defined below. In [18] the scheme (23) was rewritten and cast into the conservative formulation (21). This will be done for the present case in the next section.

A straight forward extension of the divergence-preserving flux distribution in [18] is

$$\Phi^f_{i+1/2,j} = f_{i+1/2,j}\widehat{\Phi}^f_{i+1/2,j}, \tag{24}$$

where

$$\widehat{\Phi}^f_{i+1/2,j}(k,l) = -\sum_{m=0}^{1}\sum_{n=-1}^{1} c_{mn}\Phi_{mn}(k-i, l-j), \quad c_{mn} \in \mathbb{R}, \tag{25}$$

for the flux distribution evaluated at cell (k, l) and centered at the cell edge $(i + 1/2, j)$. Here, a linear combination of the six shape functions (18) to the right are used as building block. In Fig. 2 a sketch of the distribution (25) in comparison to the one from [18] is shown. For the other flux distribution

$$\Phi^g_{i,j+1/2} = g_{i,j+1/2}\widehat{\Phi}^g_{i,j+1/2}, \tag{26}$$

we use the upper six functions,

$$\widehat{\Phi}^g_{i,j+1/2}(k,l) = \sum_{m=-1}^{1}\sum_{n=0}^{1} d_{mn}\Phi_{mn}(k-i, l-j), \quad d_{mn} \in \mathbb{R}. \tag{27}$$

The scheme in flux distribution form in [18] is obtained by translating and centering the flux distributions, corresponding to (24) and (26), around all interior cell edges and then take the sum of all contributions evaluated at the cell to be updated. By using the relation (19) we find that $\Phi_{m+s,n+t}(0,0) = \Phi_{mn}(-s,-t) = \Phi_{00}(-m-s, -n-t)$, and the scheme can be written in an equivalent form where the shape functions in (25) and (27) are evaluated also at neighboring cells and not just in their local stencil center $(0, 0)$. A generalization of the update in a divergence-preserving flux distribution scheme (23) is

$$R_{ij} = \begin{pmatrix} R^1_{ij} \\ R^2_{ij} \end{pmatrix} = \sum_{s=-k}^{k-1}\sum_{t=-k}^{k} \Phi^f_{i+1/2+s,j+t}(i,j) + \sum_{s=-k}^{k}\sum_{t=-k}^{k-1} \Phi^g_{i+s,j+1/2+t}(i,j). \tag{28}$$

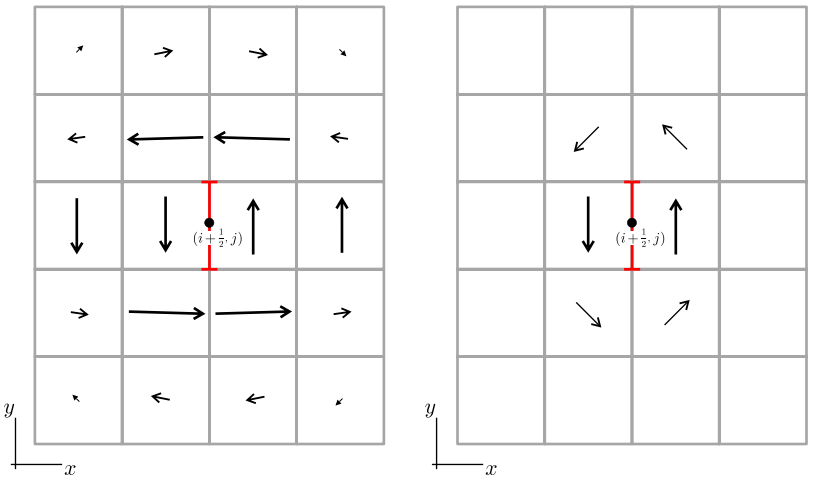

Fig. 2. Domain of influence for the flux distributions $\widehat{\Phi}^f_{i+1/2,j}$ in the fourth- (left) and second- (right) order case. The flux distributions are grid functions attached to the interface $(i + 1/2, j)$ with vector values $\widehat{\Phi}^f_{i+1/2,j}(k, l)$ in grid cells (k, l). The values are sketched as arrows in the figure, with the coefficients in the fourth-order case given by (42).

For the present 5×5-stencil we have $k = 2$ and the distributions Φ^f and Φ^g given by (24)–(27),

$$R_{ij} = \begin{pmatrix} R^1_{ij} \\ R^2_{ij} \end{pmatrix} = -\sum_{s=-2}^{1}\sum_{t=-2}^{2}\sum_{m=0}^{1}\sum_{n=-1}^{1} c_{mn}\Phi_{00}(-s-m,-t-n)f_{i+1/2+s,j+t} + \sum_{s=-2}^{2}\sum_{t=-2}^{1}\sum_{m=-1}^{1}\sum_{n=0}^{1} d_{mn}\Phi_{00}(-s-m,-t-n)g_{i+s,j+1/2+t}. \tag{29}$$

3.4. Conservative formulation

The present goal is to rewrite (23) into a conservative formulation. Because of (22) in the conservative scheme (21), we are looking for a scheme in the form

$$B^{n+1}_{ij} = B^n_{ij} - \Delta t \begin{pmatrix} (\widehat{G}_{i,j+1/2} - \widehat{G}_{i,j-1/2})/\Delta y \\ (\widehat{F}_{i+1/2,j} - \widehat{F}_{i-1/2,j})/\Delta x \end{pmatrix}. \tag{30}$$

We will focus on the derivation of $\widehat{F}_{i+1/2,j}$ and show its structure as weights in the grid for the numerical fluxes of the base scheme. These weights will be expressions of c_{mn} and d_{mn} in (25) and (27).

Consider now, for the current 5×5-stencil, the second component R^2_{ij} of (29) updating the y-component of the magnetic field. Denote by

$$\widehat{Q}_{\mathrm{st}} = \frac{1}{\Delta y}\widehat{\Phi}^{f,2}_{i+1/2+s,j+t}(i,j) \quad \text{and} \quad \widehat{P}_{\mathrm{st}} = \frac{1}{\Delta y}\widehat{\Phi}^{g,2}_{i+1/2+s,j+t}(i,j), \tag{31}$$

the scaled second components (superscript 2) of the distributions in (25) and (27). Now let

$$Q_{\mathrm{st}} = \sum_{q=s}^{1}\widehat{Q}_{qt} \quad \text{and} \quad P_{\mathrm{st}} = \sum_{q=s}^{2}\widehat{P}_{qt}, \tag{32}$$

which allow us to decompose $\widehat{Q}_{\mathrm{st}} = Q_{\mathrm{st}} - Q_{s+1,t}$, and $\widehat{P}_{\mathrm{st}} = P_{\mathrm{st}} - P_{s+1,t}$. Furthermore, due to $\sum_{q=-2}^{1}\widehat{Q}_{qt} = 0$ and $\sum_{q=-2}^{2}\widehat{P}_{qt} = 0$ independently of c_{mn} and d_{mn}, we have $Q_{\mathrm{st}} = P_{\mathrm{st}} = 0$ for $s = -2$. Using this, the residuum R^2_{ij} can be re-casted into a flux difference. We find

$$\begin{aligned}\frac{1}{\Delta y}R^2_{ij} &= \sum_{s=-2}^{1}\sum_{t=-2}^{2}(Q_{\mathrm{st}} - Q_{s+1,t})f_{i+1/2+s,j+t} + \sum_{s=-2}^{2}\sum_{t=-2}^{1}(P_{\mathrm{st}} - P_{s+1,t})g_{i+s,j+1/2+t} \\ &= \left(\sum_{s=-1}^{1}\sum_{t=-2}^{2}Q_{\mathrm{st}}f_{i+1/2+s,j+t} + \sum_{s=-1}^{2}\sum_{t=-2}^{1}P_{\mathrm{st}}g_{i+s,j+1/2+t}\right) - \left(\sum_{s=-2}^{0}\sum_{t=-2}^{2}Q_{s+1,t}f_{i+1/2+s,j+t} + \sum_{s=-2}^{1}\sum_{t=-2}^{1}P_{s+1,t}g_{i+s,j+1/2+t}\right) \\ &= \widehat{F}_{i+1/2,j} - \widehat{F}_{i-1/2,j}.\end{aligned} \tag{33}$$

So, we deduce that the distributed numerical flux is

$$\begin{aligned}\widehat{F}_{i+1/2,j} &= \sum_{s=-1}^{1}\sum_{t=-2}^{2}Q_{\mathrm{st}}f_{i+1/2+s,j+t} + \sum_{s=-1}^{2}\sum_{t=-2}^{1}P_{\mathrm{st}}g_{i+s,j+1/2+t} \\ &= -\frac{1}{\Delta y}\sum_{s=-1}^{1}\sum_{t=-2}^{2}\sum_{q=s}^{1}\sum_{m=0}^{1}\sum_{n=-1}^{1} c_{mn}\Phi^2_{00}(-q-m,-t-n)f_{i+1/2+s,j+t} \\ &\quad + \frac{1}{\Delta y}\sum_{s=-1}^{2}\sum_{t=-2}^{1}\sum_{q=s}^{2}\sum_{m=-1}^{1}\sum_{n=0}^{1} d_{mn}\Phi^2_{00}(-q-m,-t-n)g_{i+s,j+1/2+t} = \widehat{F}^f_{i+1/2,j}f + \widehat{F}^g_{i+1/2,j}g,\end{aligned} \tag{34}$$

where we have used (32) and introduced the operators $\widehat{F}^f_{i+1/2,j}$ and $\widehat{F}^g_{i+1/2,j}$; superscript 2 denotes as before the second component. Consult Fig. 3 for an illustration of the stencil for the fourth-order divergence preserving flux and a comparison to the second-order variant from [18].

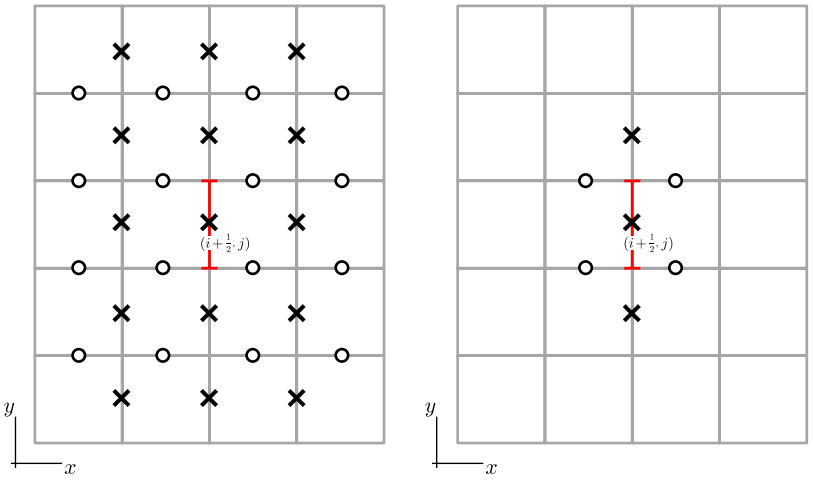

Fig. 3. Domain of dependence of a single x-flux for fourth- (left) and second- (right) order flux distribution. f- and g-fluxes enter the expression (34) according to the crosses and circles in the left figure. Their weights are given by $\widehat{F}^f_{i+1/2,j}$ (crosses) and $\widehat{F}^g_{i+1/2,j}$ (circles), see (37) and (39).

Before giving the explicit forms of the operators $\widehat{F}^f_{i+1/2,j}$ and $\widehat{F}^g_{i+1/2,j}$ we consider the distributed flux in the y-direction, updating the x-component of the magnetic field. Repeating the above derivation, now for the first component (superscript 1) of (29), we find that

$$\widehat{G}_{i,j+1/2} = \frac{1}{\Delta x}\sum_{s=-2}^{2}\sum_{t=-1}^{1}\sum_{p=t}^{1}\sum_{m=-1}^{1}\sum_{n=0}^{1} d_{mn}\Phi^1_{00}(-s-m,-p-n)g_{i+s,j+1/2+t} - \frac{1}{\Delta x}\sum_{s=-2}^{1}\sum_{t=-1}^{2}\sum_{p=t}^{2}\sum_{m=0}^{1}\sum_{n=-1}^{1} c_{mn}\Phi^1_{00}(-s-m,-p-n)f_{i+1/2+s,j+t}. \tag{35}$$

To make things explicit we first renumber the c_{mn}'s row-wise

$$\begin{aligned} &c_1 = c_{01}, \quad c_2 = c_{11},\\ &c_3 = c_{00}, \quad c_4 = c_{10},\\ &c_5 = c_{0,-1}, \quad c_6 = c_{1,-1}, \end{aligned} \tag{36}$$

and we obtain

$$\hat{F}^f_{i+1/2,j} f = \begin{array}{|c|c|c|} \hline c_6 & c_5+c_6 & c_5 \\ \hline c_4+4c_6 & c_4+4c_6+c_3+4c_5 & c_3+4c_5 \\ \hline c_2+4c_4+c_6 & c_1+c_2+4c_4+c_6+4c_3+c_5 & c_1+4c_3+c_5 \\ \hline 4c_2+c_4 & c_4+4c_1+c_3+4c_2 & 4c_1+c_3 \\ \hline c_2 & c_2+c_1 & c_1 \\ \hline \end{array} f. \tag{37}$$

The operator $\widehat{F}^f_{i+1/2,j}$ acts on the numerical flux f on the vertical cell edges $(x_{i+1/2+s}), s=-1,0,1$; cf. (34) and Fig. 3. Symmetry is now enforced by requiring the g-fluxes to play the same role for the distributed flux (35) in the y-direction as the f-fluxes do for (34) in the x-direction. This is achieved by setting the weights in (27) to $d_{mn} = c_{nm}$,

$$\begin{aligned} &d_{-1,1} = c_6, \quad d_{01} = c_4, \quad d_{11} = c_2,\\ &d_{-1,0} = c_5, \quad d_{00} = c_3, \quad d_{10} = c_1. \end{aligned} \tag{38}$$

With these numbers $\widehat{F}^g_{i+1/2,j}$ in (34) takes the following schematic form,

$$\hat{F}^g_{i+1/2,j} g = -\begin{array}{|c|c|c|c|}\hline c_1 & c_3+c_1 & c_3+c_5 & c_5 \\ \hline c_2+4c_1 & 4c_1+c_4+4c_3+c_2 & 4c_5+c_4+4c_3+c_6 & c_6+4c_5 \\ \hline 4c_2+c_1 & c_1+4c_4+c_3+4c_2 & 4c_4+c_3+4c_6+c_5 & 4c_6+c_5 \\ \hline c_2 & c_2+c_4 & c_4+c_6 & c_6 \\ \hline\end{array} g\,. \tag{39}$$

Here, the action of the stencil is on the numerical flux g on the horizontal cell edges, $(y_{j+1/2+t})$, $t=-2,\ldots,1$; cf. (34) and Fig. 3.

In the next section the weights are determined so that $\widehat{F}_{i+1/2,j}$ allows for a fourth-order accurate approximation of the first line integral (averaged) in the finite volume scheme (5).

3.5. Accuracy conditions

The divergence-preserving framework introduced in [18] can formally maintain the accuracy of a finite volume base scheme to an order p, if the redistribution of the numerical fluxes approximates the line integrals of the fluxes to this order. Below, we will determine $\widehat{F}_{i+1/2,j}$ so that the accuracy of the flux integral is maintained to fourth order. Because of (38), $\widehat{G}_{i,j+1/2}$ follows immediately by symmetry.

Since the fluxes f and g have the property $f=-g$ we will consider $\widehat{F}_{i+1/2,j}$ in (34) acting on the single function $v=f=-g$,

$$\widehat{F}_{i+1/2,j} = (\widehat{F}^f_{i+1/2,j} - \widehat{F}^g_{i+1/2,j})v. \tag{40}$$

The strategy is now to expand the 15 vertical and 16 horizontal averaged line integrals of v symmetrically in the stencil up to third order (10 terms) and under the condition that the operator (16) is preserved, requiring that the sum of the integrals approximates

$$\frac{1}{\Delta y}\int_{y_{j-1/2}}^{y_{j+1/2}} v(x_{i+1/2},\eta)d\eta = v(x_{i+1/2},y_j) + \frac{1}{24}v_{yy}(x_{i+1/2},y_j)\Delta y^2 + \mathcal{O}(\Delta^4) \tag{41}$$

to fourth order. The condition that the operator (16) is preserved is given by the stencils in (37) and (39). Putting up and solving the equations by Maple gives that the numbers

$$c_4 = c_3 = \frac{22}{576} \quad \text{and} \quad c_6 = c_5 = c_2 = c_1 = \frac{-5}{576} \tag{42}$$

in (37) and (39) make (40) a fourth-order divergence preserving approximation of the flux integral (41). Already by (37) it is clear that if a symmetric method is sought the conditions $c_4=c_3$ and $c_6=c_5=c_2=c_1$ must be fulfilled.

Putting the numbers (42) in (37) and (39) and forming (34) we find

$$\hat{F}_{i+1/2,j}\begin{pmatrix} f \\ g \end{pmatrix} = \tfrac{1}{576}\begin{array}{|c|c|c|}\hline -5 & -10 & -5 \\ \hline 2 & 4 & 2 \\ \hline 78 & 156 & 78 \\ \hline 2 & 4 & 2 \\ \hline -5 & -10 & -5 \\ \hline\end{array} f + \tfrac{1}{576}\begin{array}{|c|c|c|c|}\hline 5 & -17 & -17 & 5 \\ \hline 25 & -85 & -85 & 25 \\ \hline 25 & -85 & -85 & 25 \\ \hline 5 & -17 & -17 & 5 \\ \hline\end{array} g, \tag{43}$$

where the actions of the stencils are explained by (34). Transposing the stencils and interchanging f and g gives $\widehat{G}_{i,j+1/2}$ in (35),

$$\hat{G}_{i,j+1/2}\begin{pmatrix} g \\ f \end{pmatrix} = \frac{1}{576}\begin{array}{|c|c|c|c|c|}\hline -5 & 2 & 78 & 2 & -5 \\ \hline -10 & 4 & 156 & 4 & -10 \\ \hline -5 & 2 & 78 & 2 & -5 \\ \hline \end{array} g + \frac{1}{576}\begin{array}{|c|c|c|c|}\hline 5 & 25 & 25 & 5 \\ \hline -17 & -85 & -85 & -17 \\ \hline -17 & -85 & -85 & -17 \\ \hline 5 & 25 & 25 & 5 \\ \hline \end{array} f. \tag{44}$$

In this formula the grid functions are $f = \{f_{i+1/2+s,j+t}\}_{s=-2,t=-1}^{s=1,t=2}$ and $g = \{g_{i+s,j+1/2+t}\}_{s=-2,t=-1}^{s=2,t=1}$, cf. (35).

3.6. Second-order flux distribution as building block

It is interesting to ask if a scheme is possible that gives fourth-order accuracy for the solution, but preserves the divergence only in a second-order operator. Since a fourth-order accurate scheme requires a wider stencil, we define a flux distribution $\Phi^f_{i+1/2,j}$ which is distributing an interface flux $f_{i+1/2,j}$ to a 4×5 domain of influence. That is, we replace the 6 shape functions (18) for the construction of the flux distributions in Section 3.3 by 12 of the second-order shape functions from [18]. One of these is given in (20) and is depicted in the right hand side of Fig. 1.

The derivation of the scheme and the accuracy conditions are carried out as in the previous subsections. The results are as follows. We have 12 unknown weights c_{mn}, while consistency gives us 10 equations for fourth-order, 6 for third-order and 3 for second-order accuracy. In the second-order case the system of equations has rank 2 and is solvable. We may choose 10 weights as parameters. As a special case

$$c_{mn} = 0 \quad \text{for } (m,n) \notin \{(0,-1),(0,0)\},$$
$$c_{0,-1} = c_{00} = \frac{1}{8},$$

we recover the standard second-order divergence preserving scheme

$$\begin{aligned}\widehat{F}^{2\text{nd}}_{i+1/2,j} &= \frac{1}{8}(f_{i+1/2,j-1} + 2f_{i+1/2,j} + f_{i+1/2,j+1}) \\ &\quad - \frac{1}{8}(g_{i,j+1/2} + g_{i,j-1/2} + g_{i+1,j+1/2} + g_{i+1,j-1/2}),\end{aligned} \tag{45}$$

$$\begin{aligned}\widehat{G}^{2\text{nd}}_{i+1/2,j} &= \frac{1}{8}(g_{i-1,j+1/2} + 2g_{i,j+1/2} + g_{i+1,j+1/2}) \\ &\quad - \frac{1}{8}(f_{i-1/2,j+1} + f_{i-1/2,j} + f_{i+1/2,j+1} + f_{i+1/2,j}).\end{aligned} \tag{46}$$

Unfortunately, for the higher-order cases the system turns out to be unsolvable. Inspection of the equations shows that the coefficients for $v(x_{i+1/2}, y_j)$, $v_{yy}(x_{i+1/2}, y_j)$ and $v_{xx}(x_{i+1/2}, y_j)$ provide contradictory conditions. Dropping any single of these, gives a solvable system of rank 6. However, the result can not be third or fourth-order accurate in general.

This negative result suggests that a scheme higher than second-order accurate does not exist if we require it to preserve the second-order extended divergence operator. Also, flux distributions preserving the classical second-order divergence operator have been tried, but with analogous negative result.

3.7. Implementation

Implementing the divergence-preserving procedure of the present paper in an existing higher-order semi-discrete finite volume scheme is trivial for periodic and compactly supported problems. Other types of boundary conditions need a more careful treatment and the handling of these is a subject of future research.

Assume that, for a given finite volume base scheme, $f_{i+1/2,j}$ is the numerical flux component in the update for $(\bar{B}_y)_{ij}$ (the cell average of the magnetic field component B_y) and that $g_{i,j+1/2}$ has a similar role for $(\bar{B}_x)_{ij}$. One

possible implementation is to simply replace $f_{i+1/2,j}$ and $g_{i,j+1/2}$ by (43) and (44), respectively, for the updates in each Runge–Kutta stage. That is it. The preserved divergence operator (16) itself never enters the scheme.

The divergence preserving procedure compares very favorably to existing divergence cleaning methods, see for example [20], also regarding computational cost. In our numerical tests the observed increase in computational time was only around 2–3% compared to the pure base scheme.

4. Numerical experiments

The FV-simulations use the time step Δt determined from $\lambda\frac{\Delta t}{\Delta} = \mathrm{CFL} \leqslant 0.5$, with $\Delta = \Delta x = \Delta y, \lambda = \max\{|\sigma(f)|, |\sigma(g)|\}$ and σ denoting the eigenvalue spectrum. All simulations use CFL=0.45 and the HLLE [15] numerical flux. The adiabatic constant in the MHD-system (1)–(4) is set to $\gamma = 5/3$ in all experiments. Reconstructions are solely performed on the conserved variables.

Example 1 (*Convergence tests*). In this example empirical convergence rates for the new divergence-preserving procedure (43) and (44) are computed. Two tests are performed. In the first one, the convergence of the divergence of the magnetic field towards the divergence of the corresponding initial data (i.e. zero) is checked.

The divergence according to the preserved operator exhibits only round-off errors, so a fourth-order non-preserved operator that is constructed to obtain the point-wise divergence from known cell averages

$$C_{ij}\begin{pmatrix} u^1 \\ u^2 \end{pmatrix} = \frac{u^1_{i-1,j-1} + u^1_{i-1,j+1} + 5u^1_{i-2,j} + 36u^1_{i+1,j} - (36u^1_{i-1,j} + 5u^1_{i+2,j} + u^1_{i+1,j+1} + u^1_{i+1,j-1})}{48\Delta x} + \frac{u^2_{i-1,j-1} + u^2_{i+1,j-1} + 5u^2_{i,j-2} + 36u^2_{i,j+1} - (36u^2_{i,j-1} + 5u^2_{i,j+2} + u^2_{i+1,j+1} + u^2_{i-1,j+1})}{48\Delta y}$$

is used to demonstrate the rapid convergence towards zero for the new operator.

The second test concerns the convergence rates for the magnetic field component B_y. Empirical convergence rates for B_x have been computed as well; the results are similar and therefore omitted. To isolate the effect of the new procedure and demonstrate its higher-order convergence, the fourth-order finite volume method described in Section 2.2 is used as base scheme.

The test problem is taken from [18] and the initial conditions on $[-1,1]^2$ periodic are

$$\rho_0(x,y) = \frac{3}{2} + \frac{1}{2}\sin(\pi x) + \frac{1}{4}\cos(\pi y),$$
$$v_0(x,y) = \begin{pmatrix} 1 + \frac{1}{2}\sin(\pi y) + \frac{1}{4}\cos(\pi x) \\ 1 + \frac{1}{4}\sin(\pi x) + \frac{1}{2}\cos(\pi y) \end{pmatrix},$$
$$B_0 = \begin{pmatrix} \frac{1}{2} \\ 1 \end{pmatrix},$$
$$p_0 = \frac{1}{4}$$

and $v_z = B_z = 0$ and $\gamma = 5/3$. Cell averages of the initial data for the conserved variables are obtained by an eighth-order cross Gaussian rule. All errors are computed at $t = 0.2$ when the solution is still smooth. Table 1

Table 1
Fourth-order divergence preservation; convergence towards zero for the divergence of B according to a non-preserved fourth-order accurate divergence operator

N	L_1-error	L_1-order	L_∞-error	L_∞-order
15	4.4745e−03	–	5.9730e−03	–
30	5.1429e−04	3.1211	1.1168e−03	2.4190
60	3.8180e−05	3.7517	1.0925e−04	3.3537
120	2.4826e−06	3.9429	7.4753e−06	3.8693
240	1.5662e−07	3.9865	4.7492e−07	3.9764
480	9.8114e−09	3.9967	2.9855e−08	3.9916

shows that the new procedure fulfills its designed order for divergence preservation. As a comparison the results for the second-order operator (45) and (46) from [18] are displayed in Table 2; also this procedure shows its designed order.

For the convergence on the magnetic field components a reference solution on a 1920^2-mesh is computed using (43) and (44), since the results in [18] show that an approximation of a MHD-solution, also when smooth, obtained with a non-divergence-preserving method may exhibit large accumulated divergence errors. In Table 3 the convergence results for the new procedure are shown and we conclude that the formal order of the base scheme is respected. Table 4 gives the results for the second-order procedure (45) and (46). Now, the fourth-order base scheme shows second-order convergence, in agreement with the designed order of that divergence-preserving procedure. Tables 3 and 4 show that 60^2 cells with (43) and (44) give about the same accuracy as 480^2 cells with the procedure (45) and (46) from [18] in this convergence test.

The following numerical examples all feature discontinuous solutions and therefore the shock-capturing scheme described in Section 2.1 and Appendix A acts as base scheme in the remaining experiments.

Example 2 (*MHD Riemann problem*). In this experiment the behavior of (43) and (44) on a discontinuous solution is tested and compared to the divergence-preserving procedure (45) and (46) from [18], as well as to the non-divergence-preserving base scheme. The numerical example is used as a test case in [18] and the initial conditions are

Table 2
Second-order divergence preservation; convergence towards zero for the divergence of B according to a non-preserved fourth-order accurate divergence operator

N	L_1-error	L_1-order	L_∞-error	L_∞-order
15	1.3478e−02	–	1.7543e−02	–
30	3.1701e−03	2.0880	5.6736e−03	1.6286
60	7.3021e−04	2.1181	1.3631e−03	2.0574
120	1.7725e−04	2.0425	3.2792e−04	2.0555
240	4.3963e−05	2.0115	8.0801e−05	2.0209
480	1.0968e−05	2.0029	2.0118e−05	2.0059

Table 3
Fourth-order divergence preservation; convergence for magnetic field component B_y

N	L_1-error	L_1-order	L_∞-error	L_∞-order
15	2.5117e−03	–	4.2248e−03	–
30	1.5278e−04	4.0392	3.1442e−04	3.7481
60	8.8085e−06	4.1164	1.9913e−05	3.9809
120	5.2226e−07	4.0761	1.1855e−06	4.0702
240	3.1735e−08	4.0406	7.2020e−08	4.0409
480	1.9484e−09	4.0258	4.4234e−09	4.0252

Table 4
Second-order divergence preservation; convergence for magnetic field component B_y

N	L_1-error	L_1-order	L_∞-error	L_∞-order
15	9.2742e−03	–	1.0712e−02	–
30	2.2831e−03	2.0222	2.7511e−03	1.9612
60	5.7192e−04	1.9971	6.8762e−04	2.0003
120	1.4312e−04	1.9986	1.7245e−04	1.9954
240	3.5790e−05	1.9996	4.3152e−05	1.9987
480	8.9484e−06	1.9999	1.0791e−05	1.9996

$$\rho_0(x,y) = \begin{cases} 10, & x < 0, y < 0, \\ 1, & \text{else}, \end{cases}$$

$$p_0(x,y) = \begin{cases} 15, & x < 0, y < 0, \\ \frac{1}{2}, & \text{else}, \end{cases}$$

$$B_0 = \frac{1}{\sqrt{2}}(1,1,0)^{\mathrm{T}},$$

$$v_0 = (0,0,0)^{\mathrm{T}},$$

on $[-0.4, 0.4]^2$ with artificial absorbing boundary. A simulation with (43) and (44) using 300^2 cells is run up to $t = 0.1$. Fig. 4 shows a close up of the magnetic component B_y and the divergence on the interior of the domain as computed by the preserved operator (16). The maximal absolute value of the divergence is 1.7×10^{-12}. If the divergence is computed with the classical second-order discrete divergence operator

$$C_{ij}\begin{pmatrix} u^1 \\ u^2 \end{pmatrix} = \frac{u^1_{i+1,j} - u^1_{i-1,j}}{2\Delta x} + \frac{u^2_{i,j+1} - u^2_{i,j-1}}{2\Delta y},$$

which is not preserved, the maximal absolute value is 4.0. Note that, in all time steps the largest divergence error stays attached to a discontinuity and does not pollute the rest of the domain.

A comparison of the present procedure, the second-order one (45) and (46) and the pure base scheme is visible in Fig. 5. The left column of the figure shows a cut of the approximations to B_y at the bottom of the domain ($y = -0.4$). Here, the results of the new procedure and the base scheme appear of similar quality, while the second-order preservation exhibits a more profound undershoot at $x \approx 0.15$. In the right column, which shows a cut at $y = 0$, the effects of violation of the divergence constraint becomes clear; the base scheme approximation shows large oscillations (growing in amplitude with increasing number of cells) caused by large divergence errors. The classical divergence operator gives the maximal modulus 43; the value is assumed, not around a discontinuity, but at the origin. For the procedure (45) and (46) from [18] this value is 6.2, taken on in a neighborhood of a discontinuity, and there are no tendencies of oscillations in the approximation. The small oscillations visible in the approximation computed using the present procedure (43) and (44) do not grow in amplitude with increased number of cells; the reference solution on a 1000^2-grid is obtained by this procedure.

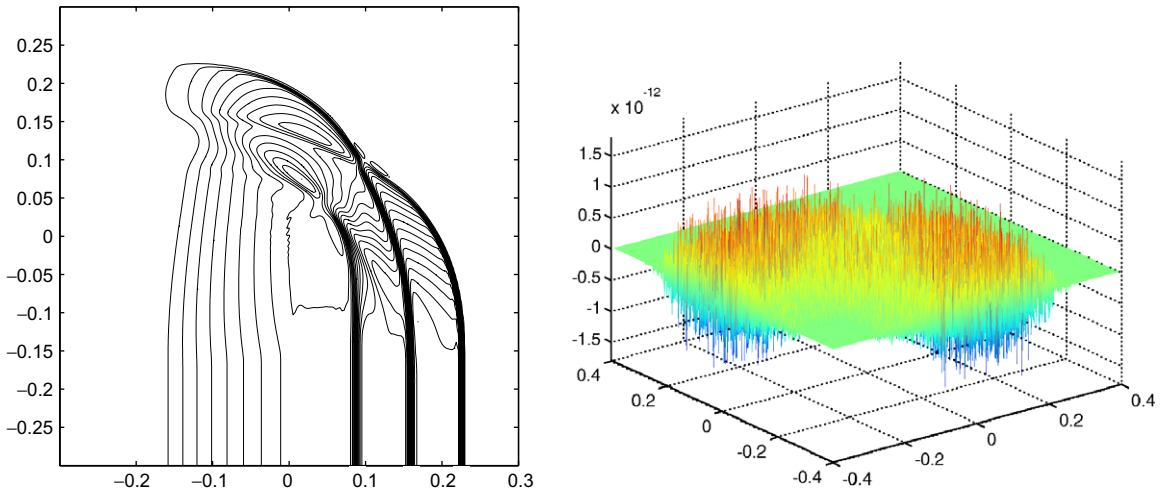

Fig. 4. Example 2. Fourth-order divergence preservation; left: 30 contours of magnetic field component B_y; right: divergence computed with the fourth-order preserved operator.

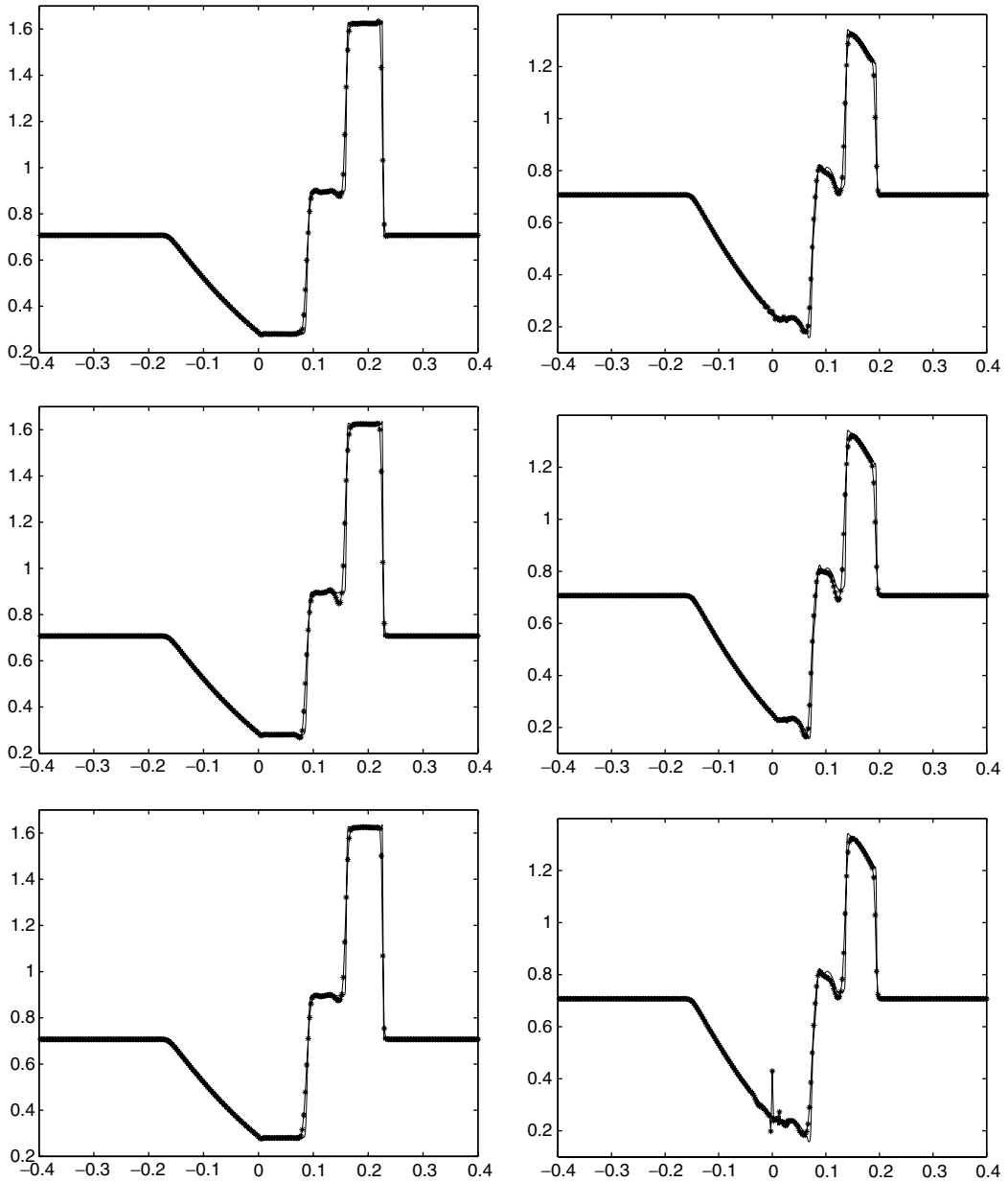

Fig. 5. Example 2. Comparison of fourth-order (top) and second-order (center) divergence preservation, and the pure base scheme (bottom); left: cut at bottom of domain; right: cut at $y = 0$. Solid line is the reference solution obtained with (43) and (44) on a 1000^2-grid.

Example 3 (*MHD Riemann problem*). The initial data for this problem are given in [6]: for (ρ, p, v_x, v_y) the four states are

$$(1, 1, 0.75, -0.5), \quad x > 0, y > 0,$$

$$(2, 1, 0.75, 0.5), \quad x < 0, y > 0,$$

$$(1, 1, -0.75, 0.5), \quad x < 0, y < 0,$$

$$(3, 1, -0.75, -0.5), \quad x > 0, y < 0,$$

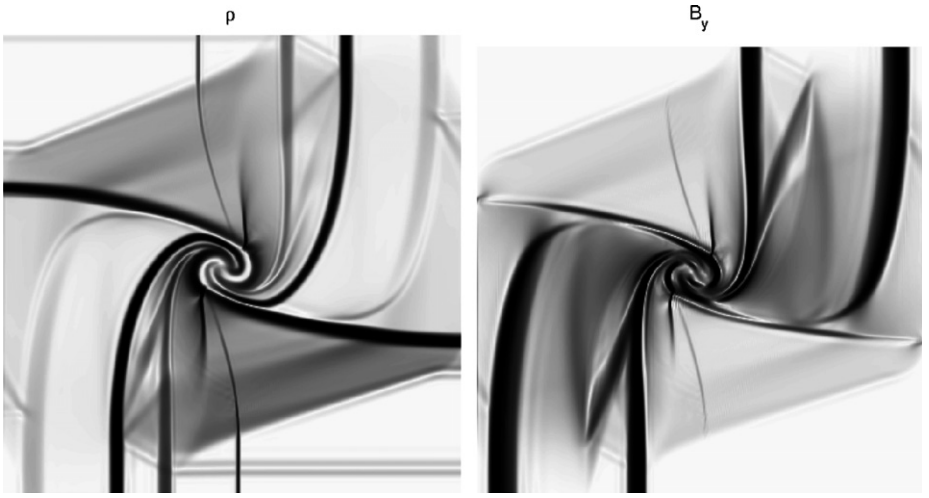

Fig. 6. Example 3. Schlieren images of density and y-component of the magnetic field for a 400×400 computation with fourth-order divergence preservation.

and the magnetic field is initially uniform $B = (2, 0, 1)/\sqrt{4\pi}$. A simulation with the fourth-order divergence-preserving procedure (43) and (44) is run on a 400^2-grid on the domain $[-1.5, 1.5]^2$ up to $t = 1$, before any discontinuity reaches a boundary. Suitable handling of the boundary is subject to future research. Fig. 6 shows schlieren images of the density and the magnetic component B_y. The maximal modulus of the divergence of (B_x, B_y) computed by the preserved operator (16) is 8.4×10^{-13}.

For this experiment and grid it was not possible to obtain an approximation with the pure base scheme; at $t = 0.93$ the scheme breaks due to negative pressure caused by large divergence errors.

Example 4 (*Orszag-Tang problem*). This well known test problem, see e.g. [20], has the initial data

$$(\rho, p, v_x, v_y, v_z, B_x, B_y, B_z) = (\gamma^2, \gamma, -\sin(y), \sin(x), 0, -\sin(y), \sin(2x), 0),$$

with $\gamma = 5/3$. The computational domain is $[0, 2\pi]^2$ periodic. The density and y-component of the magnetic field at $t = \pi$ in an approximation using the new divergence-preserving method on a 200^2-mesh are shown in Fig. 7. A simulation on a finer, 400^2, grid was also run and a schlieren image of the output for density is depicted in Fig. 8. The divergence of (B_x, B_y) computed by the preserved operator (16) is no more than 1.6×10^{-12} in absolute terms point wise. A computation with the non-divergence-preserving base scheme, however, fails at this resolution with large divergence errors before it reaches the final time.

Example 5 (*MHD Riemann problem*). This example is proposed in [7]. Initial data for the conserved variables $(\rho, \rho v_x, \rho v_y, \rho v_z, B_x, B_y, B_z, \epsilon)$ in the four quadrants are

$$\begin{aligned}
&(0.9308, 1.4557, -0.4633, 0.0575, 0.3501, 0.9830, 0.3050, 5.0838), \quad x \geqslant 0, y \geqslant 0,\\
&(1.0304, 1.5774, -1.0455, -0.1016, 0.3501, 0.5078, 0.1576, 5.7813), \quad x < 0, y \geqslant 0,\\
&(1.0000, 1.7500, -1.0000, 0.0000, 0.5642, 0.5078, 0.2539, 6.0000), \quad x < 0, y < 0,\\
&(1.8887, 0.2334, -1.7422, 0.0733, 0.5642, 0.9830, 0.4915, 12.999), \quad x \geqslant 0, y < 0,
\end{aligned}$$

on the computational domain $[-1, 1]^2$. In all numerical examples up to now, the initial configuration of the magnetic field has been free of discontinuities. The magnetic field in the present experiment however, is initialized with jump discontinuities, revealing an undesired behavior of (43) and (44), which is partly due to the negative weights in (42). Consider the lower row of Fig. 9; it shows the presence of a wave packet of high frequency oscillations, created at the discontinuity and travelling to the left.

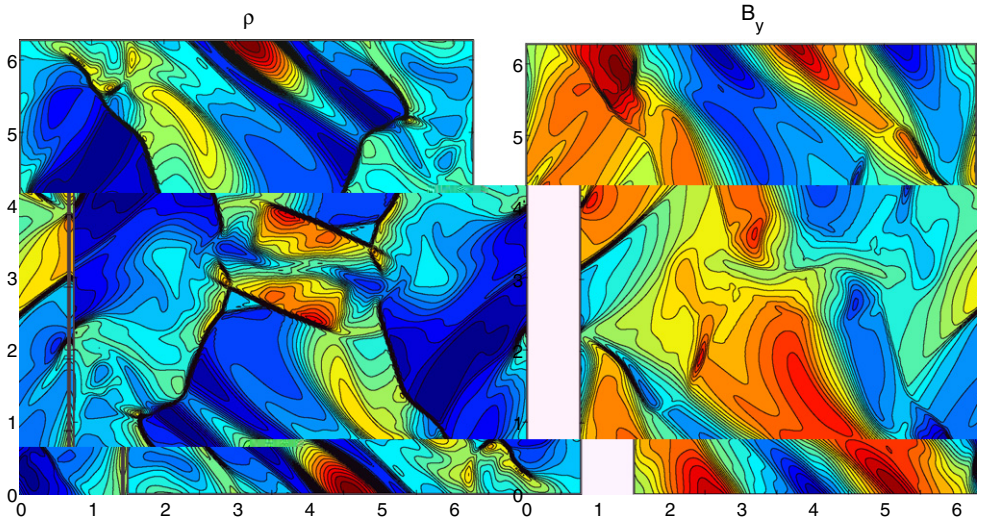

Fig. 7. Example 4. Fourth-order divergence preservation; 25 contours for density and y-component of the magnetic field for a 200×200 computation.

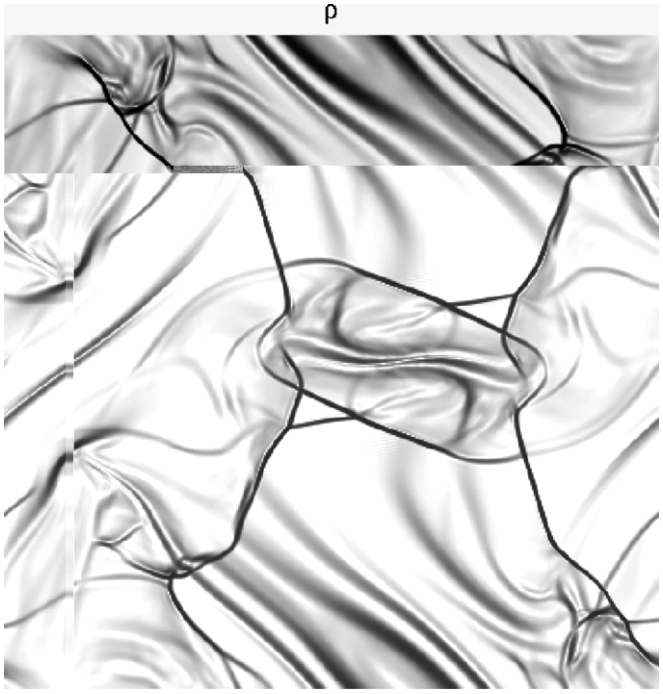

Fig. 8. Example 4. Fourth-order divergence preservation; schlieren image of density for a 400×400 computation.

Some initial smoothing of the magnetic field before invoking (43) and (44) seems to be necessary. But, as the results in Fig. 5 show, spreading the discontinuity over just a few cells appears to be sufficient; the diffusivity of the scheme will keep the approximation essentially non-oscillatory. For the initial B_y we let $a = 0.5078$ and $b = 0.9830$ be the left and right states and we smooth the discontinuity around $x = -\Delta x/2$ by putting

$$(B_y)_{n,j} = \frac{1}{2}(b-a)[1+\tanh(n+1/2)] + a \quad \text{for all } j \text{ and } n = -2, \ldots 1.$$

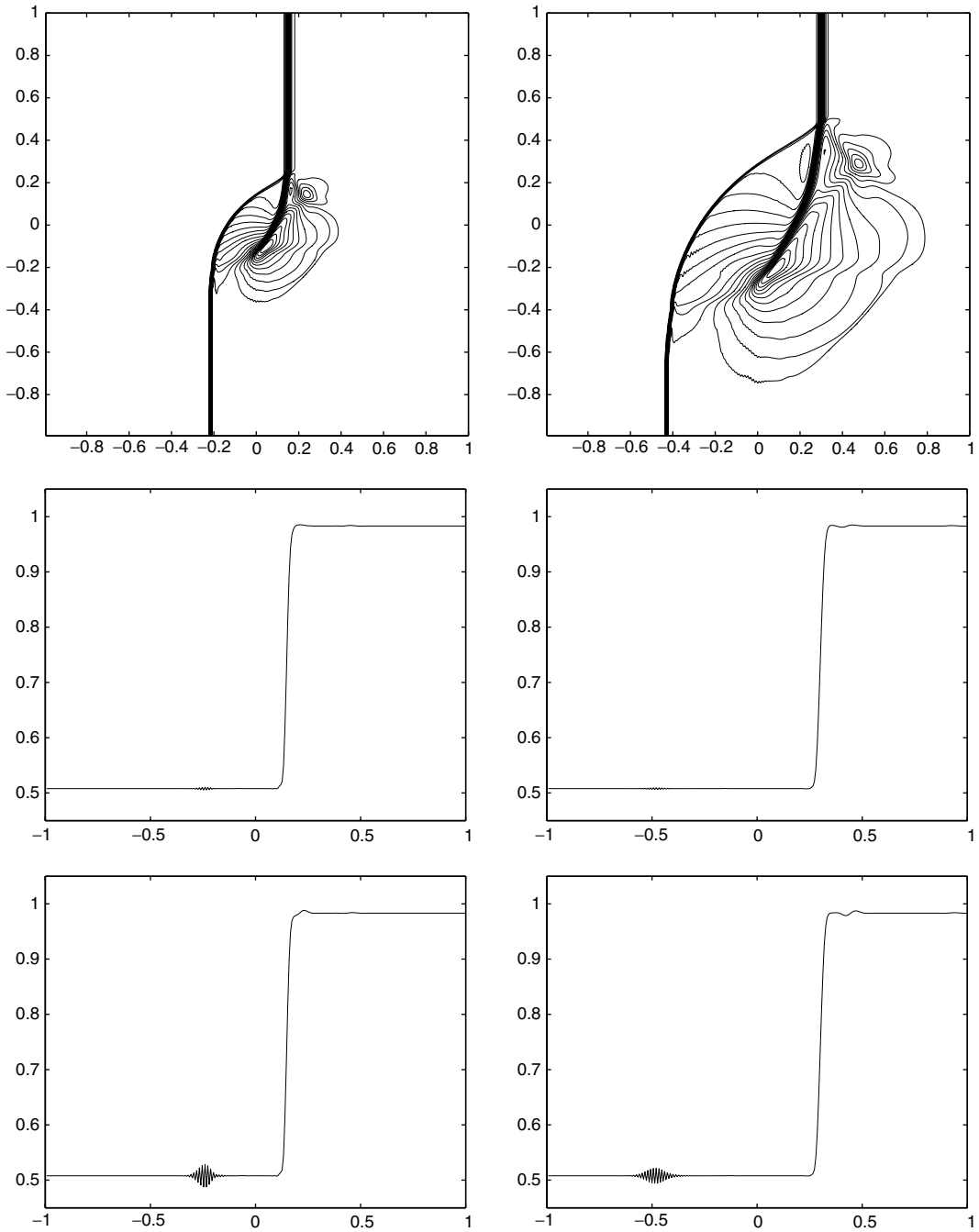

Fig. 9. Example 5. B_y-component, contours and cut at $y = 1$; left: $t = 0.125$; right: $t = 0.25$; 25 contours (top) and fourth-order divergence preservation with initial smoothing (middle) and without initial smoothing (bottom).

The initial values for B_x are modified similarly. Using the described smoothing gives the simulation results depicted in the two upper rows of Fig. 9. As visible, the oscillations are greatly reduced in amplitude. The devised approach is admittedly rather crude and more sophisticated methods to ameliorate the problem is currently under investigation.

5. Summary and conclusions

With the aim to stabilize higher-order FV-codes for MHD-simulations, this paper presented a redistribution of the numerical fluxes for (B_x, B_y) that enforces the local vanishing of a fourth-order discrete divergence operator. In doing so, the accuracy of the base scheme is maintained up to fourth order. The new procedure is a development of the second-order accurate locally divergence-preserving procedure in [18,19]. As such, it shares desirable properties: staggered grid variables are avoided, the preserved operator vanishes when applied directly to the cell averages of (B_x, B_y), and the redistribution of the numerical magnetic field fluxes is formulated in a standard conservative setting making it trivial to implement the divergence-preserving modification in an existing FV-scheme.

Numerical examples demonstrated the high accuracy and stabilizing effect. A test case uncovered that for an initially discontinuous magnetic field, prior smoothing significantly increases the approximation quality.

Appendix A. LDLR shock-capturing scheme

A.1. The LDLR coefficients

A mesh-size independent implementation of LDLR was developed in [2] and it is this implementation that is used here. Assume that we in a one dimensional setting want to reconstruct a function $u(x)$ by the LDLR reconstructing function $r_0(x)$ in the computational cell indexed 0. We do so by using the cell average $\bar{u}_0$ in this cell as well as the cell averages $\bar{u}_{-1}$ and $\bar{u}_1$ in the left and right neighboring cells. Subject to our attention in the following is the LDLR parameter

$$a = 1 - 2\frac{|d_-|^q |d_+|^q}{|d_-|^{2q} + |d_+|^{2q}}, \tag{A.1}$$

where $d_\pm = (\pm\bar{u}_{\pm 1} \mp \bar{u}_0)/h$ are the numerical derivatives, h the mesh size and $q = 1.4$. In an actual implementation (A.1) needs to be modified in order that the denominator does not vanish and it must also be assured that (A.1) does not take on the critical values zero and one, see [3,2]. To do this without introducing mesh-size dependence first rewrite (A.1) as

$$a = \frac{(m-n)^2}{m^2 + n^2},$$

with $m = |\bar{u}_0 - \bar{u}_{-1}|^q$ and $n = |\bar{u}_1 - \bar{u}_0|^q$. Now a suggestion in [9] to overcome mesh-size dependence for WENO [11] is adapted to LDLR. The algorithmic appearance of (A.1) becomes

$$a = \epsilon + (1 - 2\epsilon)\frac{(m-n)^2}{m^2 + n^2 + \mu},$$

with $\epsilon = 10^{-8}$ and $\mu = 10^{-10}\max\{\bar{u}_{-1}^2, \bar{u}_0^2, \bar{u}_1^2\}^q + 10^{-300}$. Also suggested in [2] is a less compressive alternative that is used in the present paper

$$a = \epsilon + (1 - 2\epsilon)\frac{|m-n|}{m + n + \mu}, \tag{A.2}$$

and in this case $\mu = 10^{-4}\max\{|\bar{u}_{-1}|, |\bar{u}_0|, |\bar{u}_1|\}^q + 10^{-300}$. In a two dimensional application the maximum is taken over all states in a 3×3-neighborhood of the cell under consideration and the undivided differences m and n are obtained from the appropriate numerical derivatives.

The other LDLR coefficients are

$$b = \frac{a}{a-1}, \tag{A.3}$$

$$c = \frac{(a-1)(d_+(1-b) - d_-)}{b-a}, \tag{A.4}$$

$$d = d_- - c. \tag{A.5}$$

A.2. Reconstruction on rectangles

The LDLR is a one dimensional reconstruction that in the two dimensional case is applied along the lines connecting the nodes of the 2-point Gaussian rule. Numerical derivatives at the Gaussian nodes act as input to the reconstruction. For each node two finite differences are computed and here min-mod selects the argument supplied to the LDLR, see [1] for details. For convenience the complete reconstruction on Cartesian meshes is described below.

The reconstructed point values at the points

$$z_\pm = z_0 \pm \frac{\Delta z}{2}, \quad z_{p/m} = z_0 \pm \frac{\Delta z}{2\sqrt{3}} \tag{A.6}$$

are

$$r_0(z_\pm) = c\Delta z \eta_\pm(a) + d\Delta z \eta_\pm(b), \tag{A.7}$$

$$r_0(z_{p/m}) = c\Delta z \eta_{p/m}(a) + d\Delta z \eta_{p/m}(b), \tag{A.8}$$

where

$$\eta_+(s) = -\frac{\log(1-s)+s}{s^2},$$

$$\eta_-(s) = \frac{(s-1)\log(1-s)-s}{s^2},$$

$$\eta_p(s) = \eta_-(s) + \frac{1}{s}\log\frac{6}{(\sqrt{3}+3)(3-s-\sqrt{3})},$$

$$\eta_m(s) = \eta_-(s) + \frac{1}{s}\log\frac{6}{(3-\sqrt{3})(3-s+\sqrt{3})},$$

and a, b, c, d, are the coefficients (A.2)–(A.5) with the appropriate numerical derivatives $d_\pm$, see below. To avoid two evaluations of each η-function one can exploit the fact that

$$\eta_\pm\left(b = \frac{a}{a-1}\right) = (a-1)\eta_\mp(a), \quad \eta_{p/m}\left(b = \frac{a}{a-1}\right) = (a-1)\eta_{m/p}(a).$$

The functions $\eta_\pm$ and $\eta_{p/m}$ have removable singularities at zero by putting $\eta_\pm(0) = \pm\frac{1}{2}$ and $\eta_{p/m}(0) = \pm\frac{1}{2\sqrt{3}}$, respectively. For numerical computations it is recommended to interpolate the η-functions around zero by e.g. a quadratic polynomial.

Fig. A.1 depicts the 3×3-stencil and the four LDLR-reconstructions applied in the central cell, and Table A.1 lists the numerical derivatives. For the reconstruction of $u(x, y)$ in cell O we proceed as follows

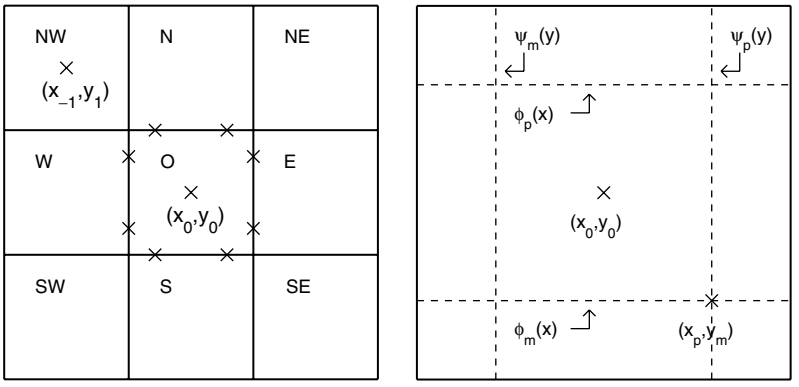

Fig. A.1. (Left) The 9-point stencil with the Gaussian nodes for cell O marked. (Right) Reconstructions $\phi_{p/m}(x)$ and $\psi_{p/m}(y)$ along the four lines.

Table A.1
Fd weights ω_i numbered clockwise starting at the upper left cell in the stencil

	FD1				FD2			
	u_x^{+p}	u_x^{+m}	u_x^{-p}	u_x^{-m}	u_x^{+p}	u_x^{+m}	u_x^{-p}	u_x^{-m}
ω_2	$\alpha = \frac{\sqrt{3}}{6\Delta x}$	β	α	β	$\gamma = \frac{6+\sqrt{3}}{6\Delta x}$	δ	γ	δ
ω_3	$\beta = \frac{6-\sqrt{3}}{6\Delta x}$	α	β	α	$\delta = -\frac{\sqrt{3}}{6\Delta x}$	γ	δ	γ
Stencil	N,NE,E,O	O,E,SE,S	NW,N,O,W	W,O,S,SW	O,E,SE,S	N,NE,E,O	W,O,S,SW	NW,N,O,W
	u_y^{p+}	u_y^{p-}	u_y^{m+}	u_y^{m-}	u_y^{p+}	u_y^{p-}	u_y^{m+}	u_y^{m-}
ω_1	$\beta = \frac{6-\sqrt{3}}{6\Delta y}$	β	α	α	$\delta = -\frac{\sqrt{3}}{6\Delta y}$	δ	γ	γ
ω_2	$\alpha = \frac{\sqrt{3}}{6\Delta y}$	α	β	β	$\gamma = \frac{6+\sqrt{3}}{6\Delta y}$	γ	δ	δ
Stencil	N,NE,E,O	O,E,SE,S	NW,N,O,W	W,O,S,SW	NW,N,O,W	W,O,S,SW	N,NE,E,O	O,E,SE,S

The stencil notation is taken from Fig. A.1 and $v_s^{ab} = (\frac{\mathrm{d}}{\mathrm{d}s}v)(x_a, y_b)$, cf. (A.6). For the x-derivatives $\omega_1 = -\omega_2$, $\omega_4 = -\omega_3$ and for the y-derivatives $\omega_4 = -\omega_1$, $\omega_3 = -\omega_2$.

Procedure A.1

(1) Compute the two different numerical lateral derivatives of $u(x,y)$ at the eight points $(x_\pm, y_{p/m})$ and $(x_{p/m}, y_\pm)$, see (A.6). The weights ω_i for the numerical derivatives, $\sum_{i=1}^4 \omega_i \bar{u}_i$, are listed in Table A.1. Let the derivative of the smallest modulus be the approximation.
(2) Find the coefficients (A.2)–(A.5) of the 1-D reconstructions $\phi_{p/m}(x)$ and $\psi_{p/m}(y)$ (cf. Fig. A.1) using the derivative approximations obtained in the previous step.
(3) Compute the averages $\mu_{p/m} = (\psi_m(y_{p/m}) + \psi_p(y_{p/m}))/2$ and $\nu_{p/m} = (\phi_m(x_{p/m}) + \phi_p(x_{p/m}))/2$ by (A.8).
(4) The reconstructed point values at the Gaussian nodes are now computed using (A.7)

$$\widetilde{u}(x_\pm, y_{p/m}) = \bar{u}_\mathrm{O} + \mu_{p/m} + \phi_{p/m}(x_\pm),$$
$$\widetilde{u}(x_{p/m}, y_\pm) = \bar{u}_\mathrm{O} + \nu_{p/m} + \psi_{p/m}(y_\pm),$$

where $\bar{u}_\mathrm{O}$ is the two-dimensional cell average in cell O.

References

[1] R. Artebrant, Third order accurate non-polynomial reconstruction on rectangular and triangular meshes, J. Sci. Comput. 30 (2007) 193–221.
[2] R. Artebrant, Reconstruction techniques and finite volume schemes for hyperbolic conservation laws, PhD Thesis, Numerical Analysis, Lund University, Lund, Sweden, 2006.
[3] R. Artebrant, H.J. Schroll, Limiter-free third order logarithmic reconstruction, SIAM J. Sci. Comput. 28 (2006) 359–381.
[4] D.S. Balsara, Second-order-accurate schemes for magnetohydro-dynamics with divergence-free reconstruction, Astrophys. J. Suppl. 151 (2004) 149–184.
[5] J.U. Brackbill, D.C. Barnes, The effect of nonzero $\nabla \cdot B = 0$ on the numerical solution of the magnetohydrodynamic equations, J. Comput. Phys. 35 (1980) 426–430.
[6] W. Dai, P.R. Woodward, A simple finite difference scheme for multidimensional magnetohydrodynamical equations, J. Comput. Phys. 142 (1998) 331–369.
[7] A. Dedner, F. Kemm, D. Kröner, C.-D. Munz, T. Schnitzer, M. Wesenberg, Hyperbolic divergence cleaning for the MHD equations, J. Comput. Phys. 175 (2002) 645–673.
[8] C.R. Evans, J.F. Hawley, Simulation of magnetohydrodynamic flows: a constrained transport method, Astrophys. J. 332 (1988) 659–677.
[9] R.P. Fedkiw, B. Merriman, S. Osher, Simplified discretization of systems of hyperbolic conservation laws containing advection equations, J. Comput. Phys. 157 (2000) 302–326.
[10] S. Gottlieb, C.-W. Shu, E. Tadmor, Strong stability-preserving high order time discretization methods, SIAM Rev. 43 (2001) 89–112.
[11] G.-S. Jiang, C.-W. Shu, Efficient implementation of weighted ENO schemes, J. Comput. Phys. 126 (1996) 202–228.
[12] G.-S. Jiang, C.-C. Wu, A high order WENO finite difference scheme for the equations of ideal magnetohydrodynamics, J. Comput. Phys. 150 (1999) 561–594.

[13] S.K. Lele, Compact finite difference schemes with spectral-like resolution, J. Comput. Phys. 103 (1992) 16–42.
[14] K.G. Powell, An approximate Riemann solver for magnetohydro-dynamics (That works in more than one dimension), ICASE Report 94-24, 1994.
[15] K.G. Powell, P.L. Roe, T.J. Linde, T.I. Gombosi, A solution-adaptive upwind scheme for ideal magnetohydrodynamics, J. Comput. Phys. 154 (1999) 284–309.
[16] J. Shi, C. Hu, C.-W. Shu, A technique of treating negative weights in WENO schemes, J. Comput. Phys. 175 (2002) 108–127.
[17] R. Spiteri, S. Ruuth, A new class of optimal high-order strong-stability-preserving time discretization methods, SIAM J. Numer. Anal. 40 (2004) 469–491.
[18] M. Torrilhon, Locally divergence-preserving upwind finite volume schemes for magnetohydrodynamic equations, SIAM J. Sci. Comput. 26 (2005) 1166–1191.
[19] M. Torrilhon, M. Fey, Constraint-preserving upwind methods for multidimensional advection equations, SIAM J. Numer. Anal. 42 (2004) 1694–1728.
[20] G. Tóth, The $\nabla \cdot B = 0$ constraint in shock-capturing magnetohydrodynamics codes, J. Comput. Phys. 161 (2000) 605–652.